

Nanosecond pulsed laser texturing of Li-ion battery electrode current collectors: Electrochemical characterisation of cathode half-cells

Original

Nanosecond pulsed laser texturing of Li-ion battery electrode current collectors: Electrochemical characterisation of cathode half-cells / Ravesio, E.; Lutey, A. H. A.; Versaci, D.; Romoli, L.; Bodoardo, S.. - In: SUSTAINABLE MATERIALS AND TECHNOLOGIES. - ISSN 2214-9937. - 38:(2023). [10.1016/j.susmat.2023.e00751]

Availability:

This version is available at: 11583/2983625 since: 2023-11-08T09:46:59Z

Publisher:

Elsevier

Published

DOI:10.1016/j.susmat.2023.e00751

Terms of use:

This article is made available under terms and conditions as specified in the corresponding bibliographic description in the repository

Publisher copyright

(Article begins on next page)



Research Paper

Nanosecond pulsed laser texturing of Li-ion battery electrode current collectors: Electrochemical characterisation of cathode half-cells

Elisa Ravesio^a, Adrian H.A. Lutey^b, Daniele Versaci^{a,*}, Luca Romoli^c, Silvia Bodoardo^a

^a Politecnico di Torino, Department of Applied Science and Technology, Electrochemistry Group, Corso Duca degli Abruzzi, 24, 10129 Turin, Italy

^b Università degli Studi di Parma, Dipartimento di Ingegneria e Architettura, Parco Area delle Scienze, 181/A, 43124 Parma, Italy

^c Università di Pisa, Dipartimento di Ingegneria Civile e Industriale, Largo Lucio Lazzarino, 56122 Pisa, Italy



ARTICLE INFO

Keywords:

Laser texturing

Aluminium current collector

LFP

Li-ion battery

ABSTRACT

Lithium-ion batteries (LIBs) have emerged as the primary energy storage solution for numerous portable electronic devices, electric vehicles, and renewable energy systems. However, enhancing the performance and longevity of LIBs is of paramount importance to meet the increasing demand for efficient and sustainable energy storage solutions.

To improve the performance of current LIBs, one of the most interesting aspects is to study and optimize the so-called inactive materials which constitute the battery.

Within this context, the present work focuses on laser texturing of aluminium current collectors (CCs) to improve the electrochemical performance of lithium iron phosphate-based cathodes. Two different nanosecond laser treatments were used to increase the wettability of metallic CCs and improve adhesion between this element and the other components of the electrode. Both laser treatments enhanced adhesion between the active material and CC, exhibiting good electrochemical performance at high C-rates compared to cells with untextured CCs, as well as good rate capability. Interestingly, one of the two pattern geometries exhibited significant cycling stability, with a capacity retention of >86% after 500 cycles.

1. Introduction

Since their introduction into the market more than thirty years ago, lithium-ion batteries (LIBs) have seen constant improvement in terms of performance, safety and cost. In a relatively short time, LIBs have become the most successful power system for a wide range of devices, from smartphones to advanced medical devices, laptops, drones, and many other common applications [1]. This progressive improvement of LIBs has led them to be among the most suitable systems for mitigating the increasing climate and energy crises [2]. Within this context, LIBs can play a fundamental role in supporting immediate action in the progressive transition towards electric mobility and better use of renewable and low environmental impact energy sources [3]. To achieve these goals in their entirety, however, further effort is required. In fact, different applications demand batteries with special requirements. For example, next-generation electric vehicles (EVs) should satisfy a mileage of >500 km, which implies LIBs with higher energy density, improved safety and longer lifespan [4]. At the same time, power grids based on short-term high-frequency energy-storage technology require

high energy density, high current charge/discharge performance, high power density and long service life [5].

It is generally accepted that improvement of battery performance requires the development of new active materials, which are directly involved in the main reversible electrochemical reaction [6]. The active material is the most important component of the battery [7], constituting 40% of the total weight. At the same time, electrochemical performance is strongly influenced by other electrode components such as the type and quantity of binder, conductive additive and current collector [8].

Focusing on the current collector (CC), this component plays multiple roles within traditional lithium-ion cells, representing about 15% of the total battery weight [7]. The main role of CCs is structural [4,10], while also ensuring easy distribution and migration of electrons to and from the active material to support high current regimes. Good contact between the current collector and other components of the electrode must therefore be guaranteed in order to facilitate rapid movement of electrons to and from the collector to the active material particles over thousands of charge/discharge cycles [4,10,11]. Furthermore, CCs must

* Corresponding author.

E-mail address: daniele.versaci@polito.it (D. Versaci).

possess excellent mechanical properties, including strength and flexibility, which allow the electrodes to be easily handled during deposition of the active material (e.g. roll-to-roll processes) and cell assembly in different cell configurations (e.g. cylindrical, prismatic or pouch).

Currently, copper (Cu) and aluminium (Al) are generally used as anode and cathode current collectors, respectively, to ensure electrochemical stability of these components [10,12]. The morphology and structural characteristics of CCs can significantly affect the overall performance of electrodes, as previously reported by several authors [4,7,15]. It has been proven that modification of the CC surface, by chemical etching or through the application of a carbonaceous coating, can improve the final performance of the battery, especially in terms of coulombic efficiency, specific capacity and capacity retention [4,11]. These improvements are mainly related to two different effects: (I) better adhesion between the active material and current collector, which guarantees good electronic transfer and, (II) the formation of a protective layer on the CC surface to limit corrosion phenomena.

Detachment of the active material from the CC is often observable during charging and discharging, in particular for materials that undergo large volumetric changes during the lithiation/de-lithiation process (e.g. silicon-based materials), causing cracks in the electrodes. This mechanical deterioration of the electrode inevitably decreases the electronic conductivity and the mobility of lithium ions, leading to fast capacity loss [12]. On the other hand, surface corrosion and chemical reactions can interfere with the normal chemistry of the battery and lead to serious safety issues [15].

Various reviews have compared different strategies for improving electrochemical performance through optimisation of the CC [7], including chemical and mechanical processes [4,11]. [16,17] Focusing on the positive electrode, one of the most common treatments involves coating aluminium with a thin layer of carbon [16] or graphene [17] to increase the performance of cells at high C-rates while inhibiting corrosion of the metal [16–18]. A second widely used treatment is chemical etching with strong acidic or basic solutions [19,20], which increases surface roughness and wettability, thus improving adhesion of the slurry and consequently improving the electrochemical performance of the electrode. However, the use of such chemical agents has a strong impact on the cost and eco-compatibility of the whole production process. Therefore, the study of more efficient, lower impact and faster methods is essential to improve the properties of current collectors.

The use of lasers in the battery production chain for cutting and welding processes has become consolidated over recent years, with lasers now widely used for cutting electrodes and separators, as well as welding different electrode sheets with appropriate tabs. Use of laser technology can also be extended to other aspects of battery production, including electrode manufacturing [21,22] or directly on the active material using nanosecond pulsed laser annealing (PLA) treatments [23,24]. Pulsed laser ablation is a viable alternative to the aforementioned coating and etching processes, with important implications in terms of battery performance and scalability to industrial manufacturing volumes.

Laser texturing of thin metallic CCs presents a unique optimisation problem in which ablation must be exploited to increase surface area while the quantity of ejected material must be limited to avoid damage. Ultrashort pulsed laser processing has potential due to the possibility of producing sub-micrometric Laser-Induced Periodic Surface Structures

(LIPSS) [25]; however, this approach is currently difficult to adopt due to limitations in terms of cost and throughput. Nanosecond pulsed laser ablation is instead a viable option due to the availability of kW-class laser sources capable of achieving industrially relevant throughput at a lower cost than ultrashort pulsed systems. This approach has been applied to much thicker current collectors than are currently employed in LIBs [26]. Optimisation of process parameters for thin metallic films remains an important issue to ensure maximum adhesion while limiting material removal via ablation.

To the authors' knowledge, a single study [25] has assessed the electrochemical performance of LIBs with laser-textured CCs, achieving promising results with ultrashort laser pulses. The aim of the present work is to study the electrochemical performance of LIB electrodes with nanosecond pulse laser textured CCs, representing a viable pathway to industrial upscaling in the short-term. A systematic study of aluminium current collector laser texturing is proposed, adopting two different texture geometries [27,28]. Textured aluminium foils are then employed as CCs for LFP-based cathodes with different mass loadings to investigate the effects of laser texturing on cell performance.

2. Materials and methods

2.1. Laser texturing of aluminium current collector

Laser texturing was performed on aluminium current collectors with a LaserPoint YFL 20P ytterbium-doped 104 ns pulsed fibre laser emitting at a wavelength 1064 nm. The maximum average power of the laser was 17 W at a repetition rate of 20 kHz, corresponding to a pulse energy of 850 μJ . Beam movement and focusing was achieved with a galvanometric scanning head equipped with a 160 mm focal length f-theta lens, achieving a focused spot diameter of approximately 60 μm ($M^2 = 1.8$) and peak pulse fluence of approximately 60 J cm^{-2} . During laser exposure, current collectors were laid out on an aluminium plate with a thin layer of distilled water applied on the underside of the films to maintain contact with the plate and avoid warping during laser exposure. All laser texturing experiments were performed with a parallel-line scanning strategy, constant laser scanning speed and constant hatch distance to achieve homogeneous surface coverage with an array of ablation craters.

A first set of experiments was performed with a scanning speed of 1.2 m s^{-1} and a hatch distance of 60 μm while varying the laser pulse fluence over a range in which ablation took place but current collectors were not damaged or perforated. This configuration led to evenly spaced craters with a separation distance equal to the focused laser spot diameter in both directions and a texturing rate of 72 $\text{mm}^2 \text{s}^{-1}$. This layout had previously been shown to achieve the highest theoretical value of the developed area ratio (*Sdr*), or fraction increase in surface area, for a given ablated volume [29], and was therefore chosen as a simple approach that required a limited number of experiments. Parameters achieving the highest value of *Sdr* while avoiding film damage were chosen for subsequent mechanical and electrochemical testing.

A second set of experiments was then performed to optimize the value of *Sdr* over a wider range of laser parameters, noting the influence of remelt and preferential heat accumulation in the scanning direction during pulsed laser ablation. In this case, laser fluence was selected based on the experimental crater depth and diameter, maximising the aspect ratio of ablation craters to achieve the greatest increase in surface area of individual craters. This outcome was achieved with an average laser power of 5 W, corresponding to a pulse fluence of 18 J cm^{-2} , leading to a crater depth of 5.4 μm , diameter of 42 μm , and aspect ratio of 0.13. Subsequently, the scanning speed and hatch spacing were varied over values ranging from 60% to 120% of the *experimental* crater diameter at the chosen pulse fluence. This configuration led to evenly spaced craters with various degrees of overlap or separation in both lateral and scanning directions and a texturing rate in the range 13–47 $\text{mm}^2 \text{s}^{-1}$. Parameters achieving the highest value of *Sdr* while avoiding

Table 1

Parameters employed for laser texturing of CCs: electrochemical testing.

Laser treatment	L1	L2
Average laser power (W)	7	5
Pulse energy (μJ)	350	250
Peak pulse fluence (J cm^{-2})	25	18
Laser scanning speed (m s^{-1})	1.20	0.80
Hatch spacing (μm)	60	46

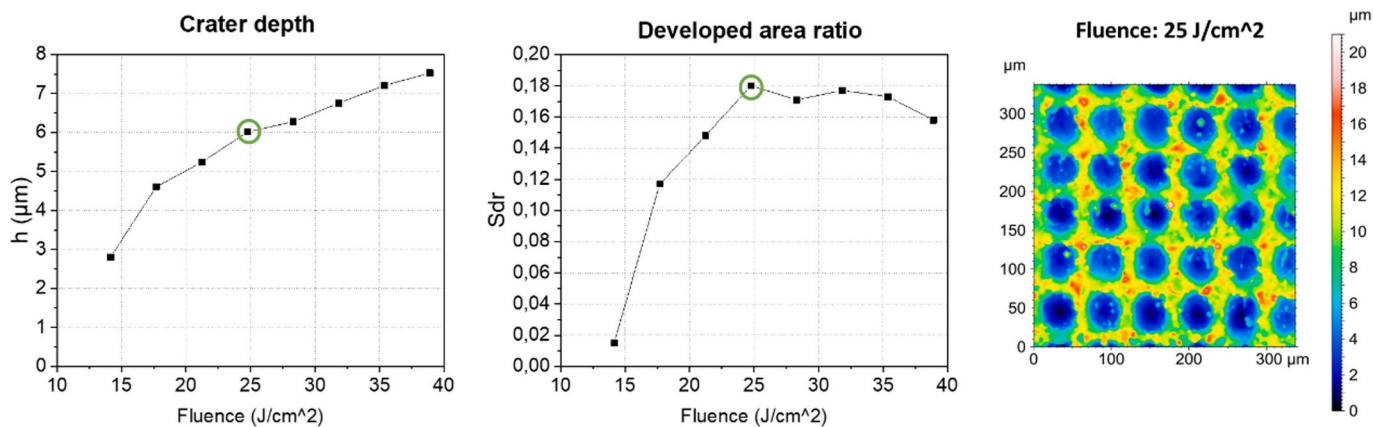


Fig. 1. Left: Crater depth and S_{dr} of laser-textured aluminium CCs (first experimental set). Right: Topography of surface indicated by green circles (7 W / 25 J cm^{-2}).

film damage were again chosen for electrochemical testing. All process parameters employed for laser texturing experiments are presented in Table S1. Process parameters leading to the highest values of S_{dr} for both sets of experiments, subsequently employed for the preparation of electrodes for electrochemical tests, are presented in Table 1.

2.2. Topography characterisation of laser-textured CCs for optimisation of process parameters

The surface topography of laser-textured CCs was acquired with a Taylor Hobson CCI-MP optical profiler equipped with a $50\times$ objective. In the employed configuration, the instrument achieved a measurement resolution of $<0.5 \mu\text{m}$ in the horizontal plane and $<1 \text{ nm}$ in the vertical direction over an acquisition area of $346 \mu\text{m} \times 346 \mu\text{m}$. For each surface, the developed area ratio, S_{dr} , was calculated. This parameter is defined as the increase in surface area with respect to the projected surface area, A_{proj} , on the mean plane:

$$S_{dr} = \frac{1}{A_{proj}} \left[\iint_{A_{proj}} \sqrt{1 + \left(\frac{\partial z(x,y)}{\partial x}\right)^2 + \left(\frac{\partial z(x,y)}{\partial y}\right)^2} dx dy \right] - 1 \quad (1)$$

In the above definition, A_{proj} is a perfectly flat surface, which was considered a reasonable representation of smooth ($S_a \approx 0.1 \mu\text{m}$) untextured current collectors. S_{dr} was therefore interpreted as the fraction increase in surface area resulting from laser texturing.

2.3. Morphology characterisation of laser-textured CCs for electrochemical testing

Contact angle measurements were carried out on the final laser-textured CCs at room temperature using a DropShape Analyzer (DSA 100 Kruss). Water droplets of volume $10 \mu\text{L}$ were deposited on current collector surfaces with a 0.60 mm diameter syringe. The measurement was repeated several times in different regions of the CCs in order to obtain a representative and reproducible value.

The morphology of the final laser-textured CCs was also assessed via FESEM with a Zeiss SUPRA TM 40 with Gemini column and Schottky field emission tip (tungsten at 1800 K). Acquisitions were made at an acceleration voltage of 3 kV and working distance (WD) of between 2.1 and 8.5 mm with magnification up to 150 kX . Sectioned electrode specimens were also prepared by laser cutting square samples of complete electrodes ($10 \text{ mm} \times 10 \text{ mm}$), which were then mounted in resin while being held vertically with a clip. Extensive lapping was performed with 80 grit abrasive paper to remove the cut edge prior to lapping with finer abrasive paper and polishing with $1 \mu\text{m}$ diamond particles in suspension.

2.4. Cathode preparation and electrochemical characterisation

Working electrodes were prepared by the solvent tape casting method. An aqueous based cathodic slurry was prepared by mixing lithium iron phosphate (LFP, ALEES), Carbon Black C-NERGY C45 (Imerys Graphite & Carbon Corporation) and sodium carboxy methyl cellulose Na-CMC (DAICEL) at a weight ratio of $85:10:5 \text{ wt\%}$, respectively. For preparation of the slurry, Na-CMC was dissolved in deionized water to obtain 5 wt\% solutions. After complete binder dissolution, the solid fraction (active material + carbon black) was added to the solution and the slurries were homogenized using a ball mill for 15 min at 30 Hz . Subsequently, the obtained slurries were cast onto pristine and laser-textured aluminium current collectors (battery grade) by the Doctor Blade technique using an automatic film applicator (Sheen 1133 N, speed of 50 mm s^{-1}). Different wet deposition thicknesses (from 100 to $300 \mu\text{m}$) were set to obtain different electrode mass loadings, as reported in Table 4.

After solvent evaporation in air at $50 \text{ }^\circ\text{C}$ for 1 h , 1.766 cm^2 disks were punched out with a Compact Precision Disc Cutter MSK-T-07 and vacuum dried at $120 \text{ }^\circ\text{C}$ (Büchi Glass Oven B-585) for 4 h prior to cell assembly.

Cell assembly was carried out in an Ar-filled glove box (MBraun Labstar, H_2O and O_2 content $<1 \text{ ppm}$) using a two-electrode 2032 coin cell configuration. Glass fibre (Whatman GF/D) was used as a separator and soaked with an electrolyte solution of LiPF_6 1 M $1:1 \text{ v/v}$ mixed with ethylene carbonate (EC) and diethyl carbonate (DEC) (Solvionic).

LFP cathodes were electrochemically tested at RT using Li disk counter electrodes ($\varnothing 16 \text{ mm}$, thickness 0.6 mm , Tobmachine). The cycling performance of cells was assessed through galvanostatic discharge-charge cycling (GC) on an Arbin LBT-21084 at different current regimes in the voltage range $2.5\text{--}4 \text{ V}$. Electrochemical impedance spectroscopy (EIS) characterisation was conducted on a versatile multichannel potentiostat (VMP-3 Biologic). Impedance measurements were performed after different cycles of charge-discharge at 0.1C with a 10 mV amplitude in the $100 \text{ kHz}\text{--}100 \text{ MHz}$ frequency range.

3. Results and discussion

3.1. Topography characterisation of laser-textured CCs for optimisation of process parameters

The average crater depth and developed area ratio (S_{dr}) of laser-textured aluminium CCs obtained during the first set of experiments (Table S1) are presented in Fig. 1. The crater depth increased in an approximately logarithmic manner with laser pulse fluence, while the value of S_{dr} took on a maximum value at 25 J cm^{-2} . As pulse fluence increased from low to moderate values, the depth and width of craters

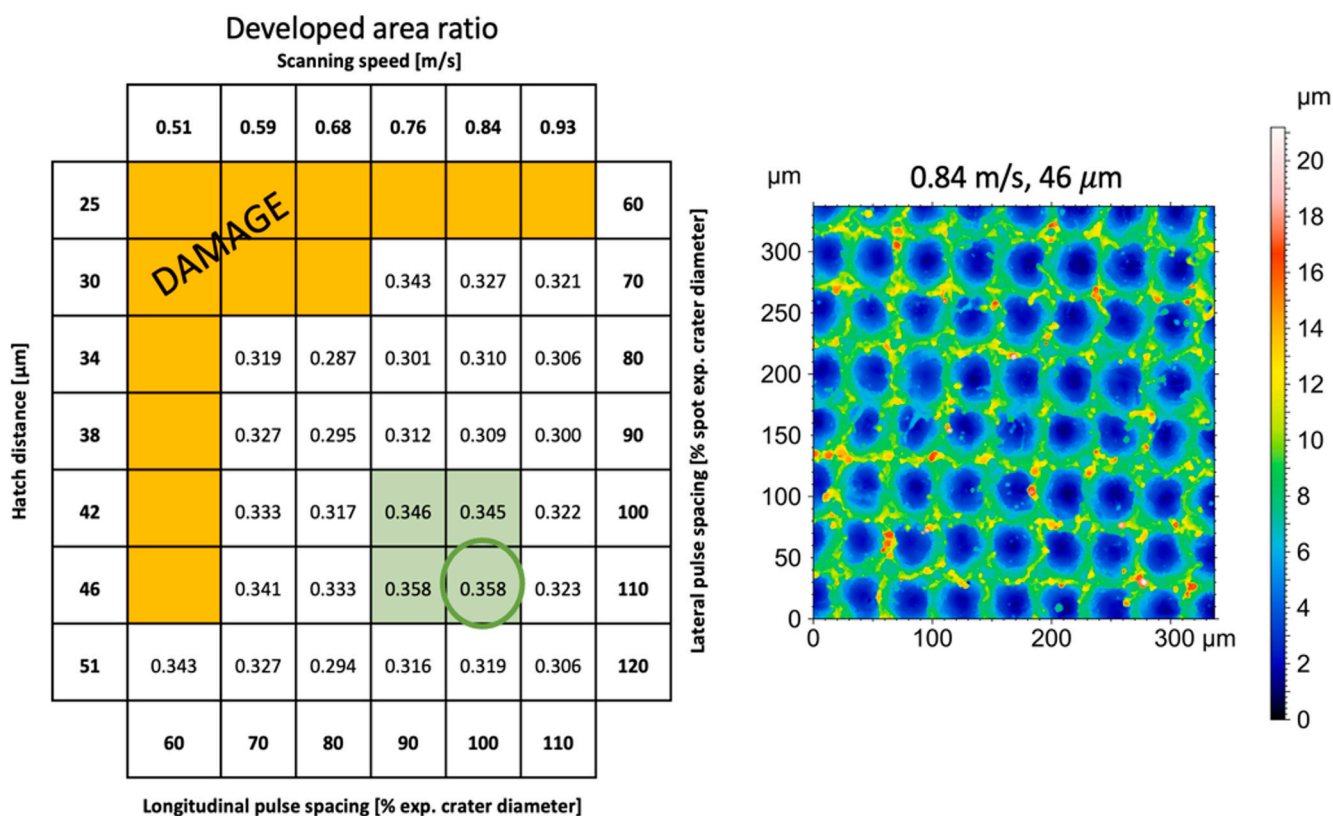


Fig. 2. Sdr of laser-textured aluminium CCs (second experimental set), together with acquired surface topography of surface indicated by green circle (0.84 m s^{-1} , $46 \mu\text{m}$).

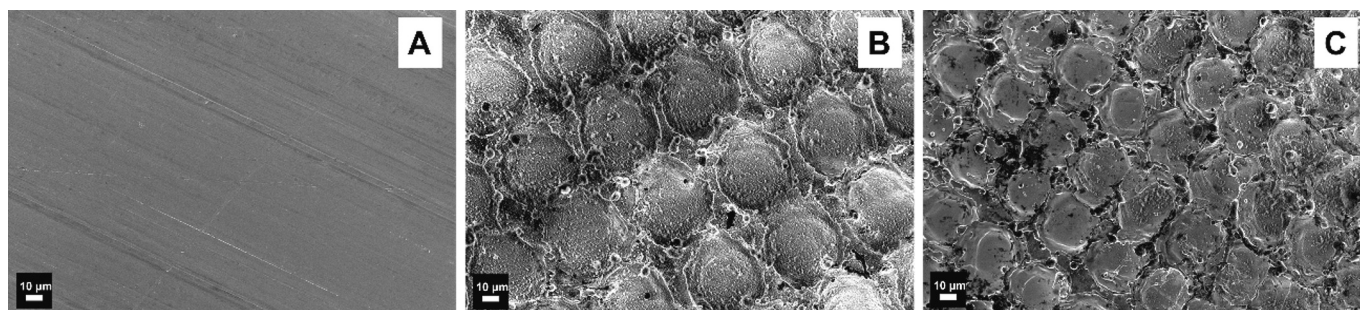


Fig. 3. FESEM micrographs of pristine current collector (A), L1 current collector (B), L2 current collector (C).

increased, leading to increases in surface area and therefore Sdr . At high pulse fluence, however, increased material ejection and melting led to amalgamation of adjacent ablation craters, inhibiting further increases in Sdr above 25 J cm^{-2} . Optimal process parameters for this set of experiments were therefore considered those leading to maximum Sdr . These conditions are indicated by green circles in Fig. 1, corresponding to an average laser power of 7 W and pulse fluence of 25 J cm^{-2} , achieving an increase in surface area of 18% ($Sdr = 0.18$). A topography map of the surface is shown in the right part of Fig. 1, where regular arrays of ablation craters can be observed, with raised ridges resulting from expansion of molten material during laser exposure. These parameters were employed for subsequent electrochemical testing (L1, Table 1).

Results of the second set of laser texturing experiments are summarised in Fig. 2, where the laser pulse fluence was chosen to maximise the aspect ratio of individual craters and the scanning speed and hatch distance were chosen to achieve pulse spacing in the range 60–120% of the experimental crater diameter (Table 1). Optimisation of laser

processing parameters in this way led to further increases in the surface area, up to 35.8% ($Sdr = 0.358$). Highest values of Sdr were achieved where the pulse spacing was similar to the experimental crater diameter in both directions (0.84 m s^{-1} , $46 \mu\text{m}$). These parameters were therefore employed for subsequent electrochemical testing (L2, Table 1).

3.2. Morphology characterisation of laser-textured CCs for electrochemical testing

Field Emission Scanning Electron Microscopy (FESEM) and Energy Dispersive Spectroscopy (EDS) analyses were conducted on both pristine CCs and the final laser-textured current collectors (L1 and L2) prepared with the parameters given in Table 1. Fig. 3 shows a comparison of the most representative micrographs.

As can be seen in Fig. 3a, the pristine current collector had a very homogeneous and flat surface. In contrast, both current collectors that underwent laser treatment exhibited crater-like structures resulting from the ablation process. Differences between the two laser treatments

Table 2

Results of EDS analyses performed on pristine and laser-textured aluminium current collectors.

Element	Pristine	L1	L2
	%	%	%
Aluminium	100.00	93.94	95.46
Oxygen	–	6.06	4.54

were more pronounced at low magnification (1.00 kX). Specifically, the morphology of the current collector treated with the first set of parameters (L1) was more uniform, with equidistant craters and well-defined edges. In contrast, the current collector treated with the second set of parameters (L2) had a less uniform surface morphology due to a smaller distance between features, which led to partial collapse of the crater-like structures. At higher magnification (e.g., 20 kX), it was possible to better evaluate the internal morphology of the laser-induced craters. For the CC treated with the first laser treatment (L1), the internal surface of craters was homogeneous with a sponge-like morphology. However, the morphology was quite different for the CC treated with the second set of parameters (L2). In this case, most of the craters exhibited an undefined structure, which created a higher level of disorder on the CC surface. This effect may have been due to the lower pulse fluence employed in the second case, leading to weaker ejection of the molten phase, as well as the smaller hatch spacing, causing an excess of local heat accumulation responsible for the partial coalescence of craters. The noticeable morphological difference between the surfaces of the two treated current collectors influenced the adhesion of the active material and, consequently, the electrochemical performance of the electrodes.

The elemental surface composition of the same CCs was evaluated by EDS analysis, with results reported in Table 2. As expected, the pristine current collector was composed of pure aluminium (100%). This elemental composition is typical of commercial aluminium used for batteries and supercapacitors. On the other hand, EDS analysis of the L1 and L2 CCs revealed an increase in the quantity of oxygen. This increase was likely due to the high-energy laser treatment, causing oxidation on the aluminium surface. In this case, the measured oxygen increased to 6.06% and 4.54%, while the detected aluminium decreased to 93.94% and 95.46%, respectively.

The measured oxygen content was likely due to the formation of a nanoscale Al_2O_3 passive layer [6] or traces of $\text{Al}(\text{OH})_3$ [25,26] originating from the production process and exposure to air. It is worth noting that a controlled and thin oxidised layer of Al_2O_3 can protect the aluminium surface from various corrosion phenomena. In particular, a stronger protective layer is formed when the charge/discharge process of the LIB is conducted in the presence of electrolytes with fluorinated compounds such as LiPF_6 , as demonstrated in various studies [26,27]. A thin oxide layer can therefore increase the internal resistance of the system slightly, but at the same time play a fundamental role in long-term electrochemical performance of the LIB, limiting the electrode degradation process and extending the cycle-life of the battery.

In addition to differences in chemistry, the surface morphology of CCs strongly influenced water wettability, as is evident from the contact angle measurements shown in Fig. 4. According to wettability theory, a

material with a contact angle $<90^\circ$ is considered hydrophilic, implying that all three CCs were hydrophilic [30]. However, there was a significant difference between the pristine CC and the two laser-treated CCs. The contact angle for pristine aluminium (Fig. 4A) was close to 62° , consistent with other studies [28], while that of the laser-textured CCs was $<5^\circ$. This behaviour was attributed to the crater-like surface of the two laser-treated aluminium foils and consequent increase in surface area, or Wenzel roughness factor [31], with fundamental implications for aqueous slurry processes. In fact, as mentioned in previous papers [32,33], in the case of water-based slurries, a reduction in surface tension corresponds to a decrease in the contact angle. This, in turn, results in improved wettability of the solvent on the aluminium collector. Moreover, a lower surface tension helps mitigate issues associated with electrode delamination [33] and some current collector surface treatments, such as laser treatment, result in a rougher surface, enhancing the hydrophilic properties of the CC [34,35]. Increased wettability has also been linked to improved electrochemical performance [19,20].

In light of the observations obtained for the different current collectors in terms of morphology and wettability, the three CCs were used to manufacture LFP-based electrodes. Considering the results obtained in terms of water contact angle and the importance of a production process with low environmental impact, an aqueous-based slurry formulation was preferred. The same slurry deposition parameters were used for all electrodes in terms of AM:CB:binder ratio, solid fraction, deposition speed, mixing time, etc., with only the blade thickness changed. This was done so as to better evaluate the role of current collector morphology on the final electrode mass loading, as reported in Table 3.

Using an initial blade thickness of $100\ \mu\text{m}$, both electrodes with laser-textured CCs exhibited higher mass loading. The average mass loading of the pristine electrode was $1.8\ \text{mg cm}^{-2}$, which was lower than the average values of 2.1 and $2.3\ \text{mg cm}^{-2}$ obtained for the LFP_L1 and LFP_L2 electrodes, respectively. At the same time, the electrodes with textured CCs exhibited a lower final thickness, 30% and 18% less than the electrode with pristine CC, respectively.

Increasing the blade thickness to $300\ \mu\text{m}$, the pristine CC electrode exhibited a mass loading of approximately $6.1\ \text{mg cm}^{-2}$. A similar value was observed for the electrode with laser-textured CC subject to the first parameter set (L1), while a mass loading of $6.9\ \text{mg cm}^{-2}$ was obtained for the electrode with laser-textured CC subjected to the second parameter set (L2).

Electrodes obtained with laser-treated CCs also exhibited lower electrode thickness in this case, about 21% lower than that observed for

Table 3

Average mass loading values calculated on the basis of the different imposed Doctor Blade thicknesses.

Thickness (μm) of the wet slurry	Mass Loading (mg cm^{-2})			Active Material Thickness (μm)		
	LFP_P*	LFP_L1*	LFP_L2*	LFP_P*	LFP_L1*	LFP_L2*
100	1.8	2.1	2.3	50	35	41
300	5.7	6.1	6.9	99	81	80

* P = pristine, L1 = Laser 1 treatment, L2 = Laser 2 treatment.

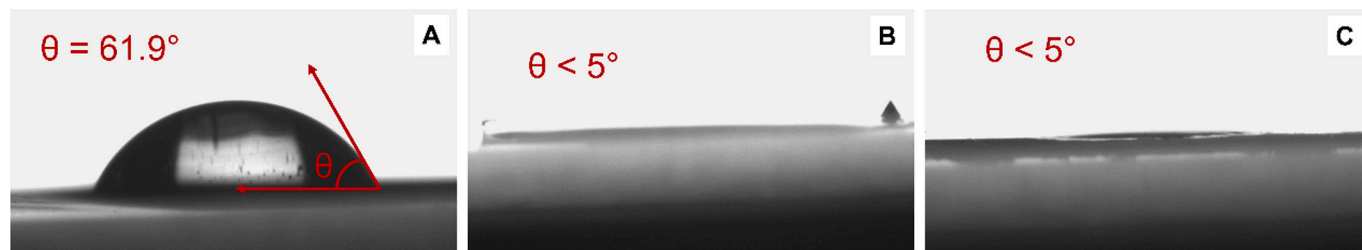


Fig. 4. Contact angle measurement of pristine current collector (A), L1 current collector (B), L2 current collector (C).

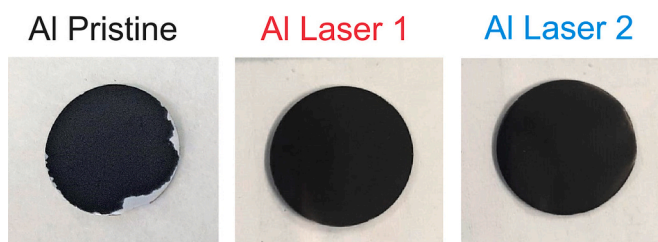


Fig. 5. Pictures of cut electrodes obtained by applying slurry on pristine and laser-textured current collectors (imposed thickness of 300 μm).

the cathode employing a pristine aluminium foil. These values imply that by adopting laser treatment, it is possible to increase the mass loading, reducing the final thickness of the electrode. This outcome is likely due to material removal from the CC during the laser-texturing process. This aspect is particularly important in terms of volume occupation, with important consequences for the final volumetric energy density of the cell.

The creation of craters on the surface of the collector reduced the collector's thickness in favour of a greater thickness of active material (inside craters). This approach allowed electrodes to be achieved with higher mass loading under identical coating conditions (slurry formulation, blade height, and drying process) when using the laser-textured CC. From a battery production perspective, this represents a significant aspect of the electrode manufacturing process, as it enables the current collector thickness and mass to be reduced, potentially leading to improvements in energy and volumetric density in the final cell.

A second fundamental aspect affecting electrode performance is adhesion of the active material to the CC. As shown in Fig. 5, the electrode with pristine aluminium exhibited partial detachment of the active

material after cutting, which was particularly evident along the edges of the disk. In contrast, adhesion of the active material was fully maintained on both electrodes with laser-treated CCs, even after stresses induced by the cutting process.

To better illustrate the distribution of the active material within craters on the surfaces of laser-textured CCs, SEM analysis was carried out on electrode cross-sections, presented in Fig. S1. In general, a homogeneous and continuous distribution of the active material was observed along CC surfaces for all samples. The surface of the laser-treated CC (L1) confirmed the presence of a homogeneous crater-like texture with ridges and depressions responsible for improved adhesion of the active material to the CC. The active material penetrated into craters on the aluminium foil, resulting in complete contact between the carbon black and current collector. This good distribution of the active material was considered the basis for the increase in mass loading of the electrodes obtained using laser-textured aluminium foil.

The thickness of the active material was calculated from the acquired images, confirming the data measured with the thickness gauge reported in Table S1 of the Supporting Information. Considering sample LFP_P (imposed blade thickness of 100 μm), the average thickness of the active material calculated from SEM images was about 47 μm , which was in alignment with the average value of 50 μm reported in Table 2. On the other hand, for LFP_L1 (imposed blade thickness of 300 μm), the current collector exhibited an average thickness of 16.8 μm in correspondence with each crater, implying a depth in the range of approximately 6–8 μm .

3.3. Electrochemical characterisation

Prepared electrodes were subjected to detailed electrochemical characterisation in a half-cell configuration using lithium metal as the counter electrode. The cycling performance of prepared cells was

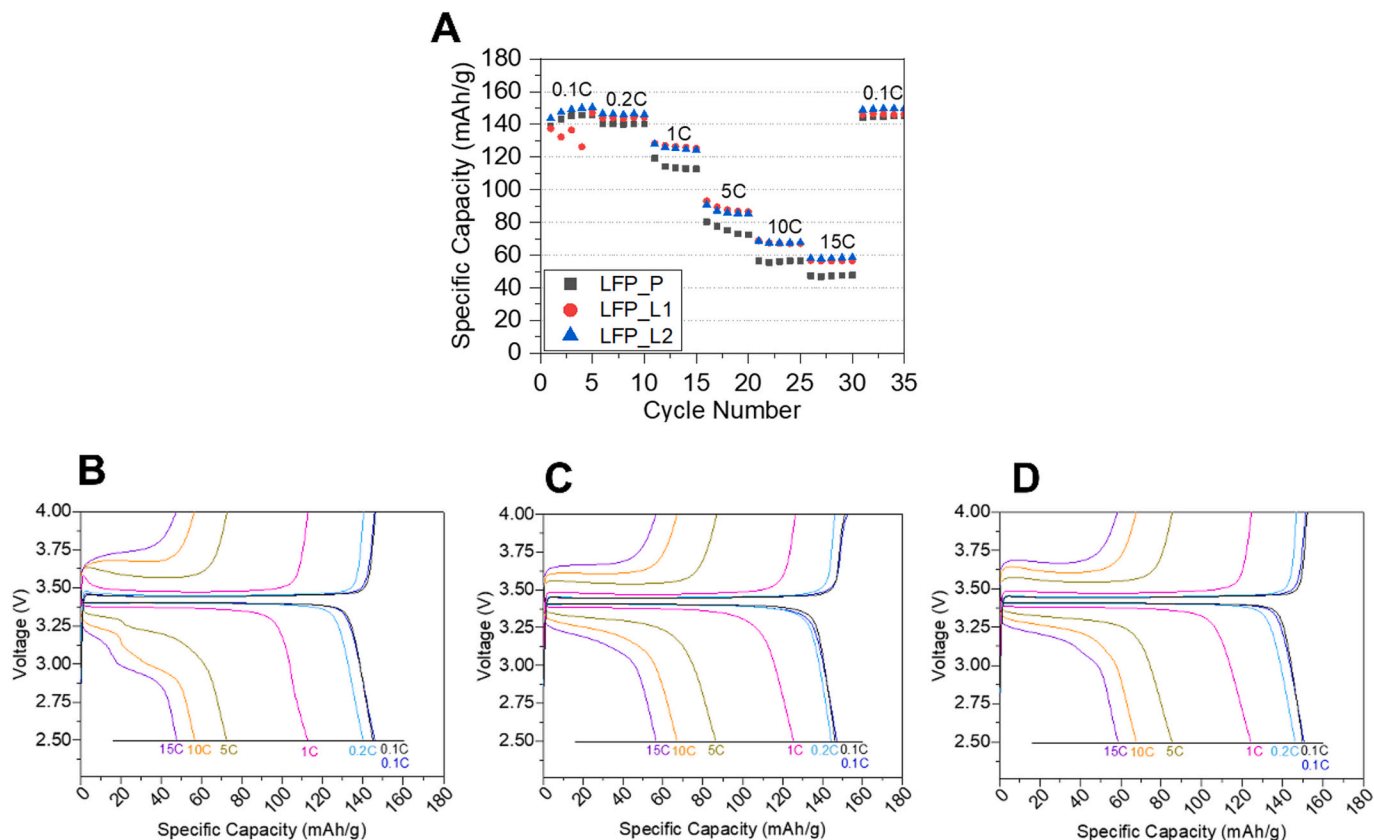


Fig. 6. Rate capability of the three CCs at low mass loading (2–3 mg cm^{-2}) (A), charge/discharge curves for LFP_P (B), charge/discharge curves for LFP_L1 (C), charge/discharge curves for LFP_L2 (D).

Table 4
 Values of discharge capacity, coulombic efficiency and rate capability of electrodes prepared with the three different CCs at different C-rates.

		Cycle Number	C-Rate	Discharge Capacity mAh g ⁻¹	Coulombic Efficiency %	Capacity retention %			Cycle Number	C-Rate	Discharge Capacity mAh g ⁻¹	Coulombic Efficiency %	Capacity retention %		
Low Mass Loading	LFP_P	1	0.1C	139.2	93.2		High Mass Loading	LFP_P	1	0.1C	146.8	94.2			
		2		143.3	100.0				2		145.4	94.6			
		3		145.3	100.0				3		149.6	94.1			
		5		145.8	100.0				5		143.3	81.0			
		10	0.2C	140.2	99.9	96.1			10	0.2C	146.6	95.6	100.0		
		15	1C	112.7	99.9	77.3			15	1C	126.7	99.3	86.4		
		20	5C	72.5	99.8	49.7			20	5C	78.1	98.9	54.5		
		25	10C	56.7	100.0	38.9			25	10C	51.6	100.0	36.0		
		30	15C	47.8	100.0	32.8			30	15C	33.1	100.0	23.1		
		35	0.1C	149.4	98.5	100.0			35	0.1C	150.2	93.7	100.0		
		LFP_L1	1	0.1C	137.4	90.8				LFP_L1	1	0.1C	148.7	95.9	
			2		132.3	80.3					2		151.2	100.0	
			3		136.5	65.0					3		152.1	100.0	
			5		146.9	96.4					5		152.4	99.9	
			10	0.2C	144.2	98.6			98.2		10	0.2C	145.8	99.9	95.7
	15		1C	125.4	99.3	85.4	15	1C	119.9		99.3	78.7			
	20		5C	86.5	99.6	58.9	20	5C	75.1		99.4	49.3			
	25		10C	67.1	100.0	45.7	25	10C	54.1		100.0	35.5			
	30		15C	56.6	100.0	38.5	30	15C	35.4		100.0	23.2			
	35		0.1C	146.2	96.7	99.5	35	0.1C	149.4		98.5	98.0			
	LFP_L2		1	0.1C	143.7	93.8		LFP_L2	1		0.1C	142.7	96.7		
			2		147.4	100.0			2			142.6	98.9		
			3		149.0	100.0			3			146.2	100.0		
			5		150.4	99.3			5			147.6	99.7		
			10	0.2C	145.9	99.4	97.0		10		0.2C	141.8	98.4	96.1	
		15	1C	124.2	99.7	82.6	15		1C	113.6	99.3	77.0			
		20	5C	85.3	99.9	56.7	20		5C	68.9	99.5	46.7			
		25	10C	67.7	100.0	45.0	25		10C	45.5	100.0	31.0			
		30	15C	58.6	100.0	39.0	30		15C	19.1	100.0	12.9			
		35	0.1C	149.8	98.5	99.6	35		0.1C	148.1	98.6	100.0			

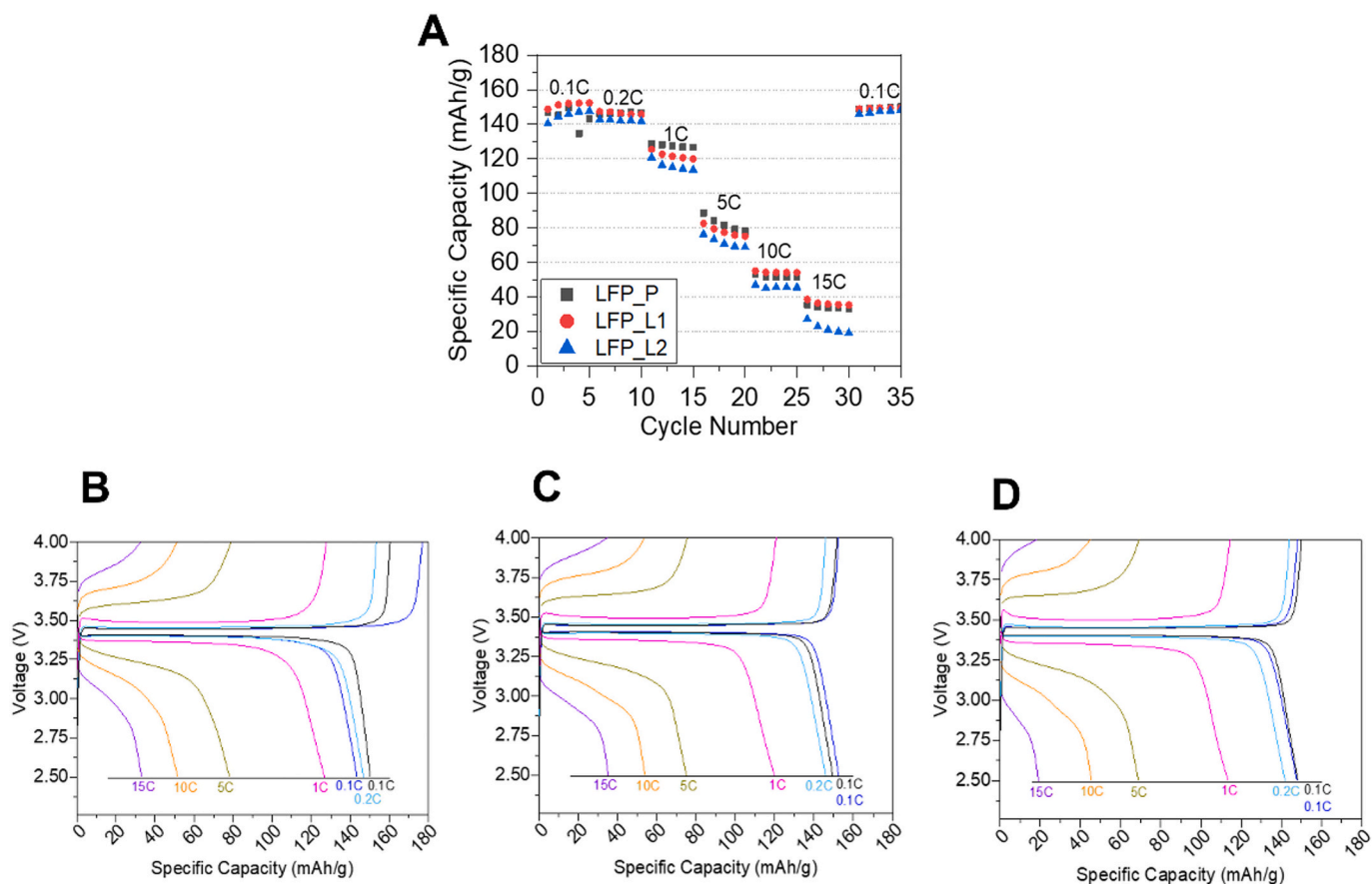


Fig. 7. Rate capability of the three CCs at low mass loadings ($6\text{--}7\text{ mg cm}^{-2}$) (A), charge/discharge curves for LFP_P (B), charge/discharge curves for LFP_L1 (C), charge/discharge curves for LFP_L2 (D).

initially characterised in terms of rate capability. Electrodes with low mass loading ($2\text{--}3\text{ mg cm}^{-2}$) and high mass loading ($6\text{--}7\text{ mg cm}^{-2}$) were subjected to repeated charge and discharge cycles at different C-rates (0.1C, 0.2C, 1C, 5C, 10C, 15C).

By comparing the electrochemical results of electrodes with lower mass loading (Fig. 6), the electrodes with treated and untreated CCs exhibited similar specific capacity values at low current (e.g. 0.1C and 0.2C). The specific capacity of the first cycle at 0.1C was comparable for all the three samples: 139 , 137 and 144 mAh g^{-1} for LFP_P, LFP_L1 and LFP_L2, respectively (Table 4). The specific capacity continued to remain comparable after five forming cycles performed at 0.1C, with values ranging from 145 to 150 mAh g^{-1} .

It is worth noting that initial forming cycles are susceptible to variations, as highlighted by the behaviour observed for LFP_L1. This phenomenon may arise from the permeation and wettability processes of the electrolyte within the porosity of the electrode. It is possible that certain areas of the electrode require more time and gradual charge/discharge cycles to undergo activation. This effect may be more pronounced in thicker and/or denser electrodes.

On the contrary, at higher C-rates the electrodes with laser-textured CCs exhibited higher specific capacity. In particular, LFP_P exhibited a specific capacity of 112 mAh g^{-1} at 1C, which was lower than values observed for LFP_L1 (124 mAh g^{-1}) and LFP_L2 (125 mAh g^{-1}). This trend was maintained at C-rates higher than 1C. For instance, at 5C, LFP_P exhibited a specific capacity of 72 mAh g^{-1} while LFP_L1 and LFP_L2 obtained values of 86 and 85 mAh g^{-1} , respectively. Increasing the C-rate up to 15C, the specific capacity of LFP_P remained the lowest, with a value of 47 mAh g^{-1} , while LFP_L1 and LFP_L2 exhibited specific capacities that were 18% and 22% higher, respectively.

This behaviour can be attributed to better distribution of the active

material on laser-textured CCs. In particular, an aluminium surface characterised by craters leads to an increase in roughness and a larger contact area [28], ensuring better distribution and electric charge transfer between the CC and active material. The laser-induced surface modification essentially creates a 3D structure that permits faster electron transfer while also guaranteeing optimal electrolyte wettability and ion diffusion.

This effect is particularly evident in Fig. 6 (B–D), where charge/discharge curves at different C-rates are reported for each type of CC. As can be observed, the charge/discharge profiles were very similar for the three samples at low C-rates, while pronounced differences between the samples become evident at higher current regimes ($> 5C$), where distinct overpotential values emerge. Upon closer examination of the profiles, a notable feature is the increased separation (polarisation) between the charging and discharging curves for the LFP_P electrode. Additionally, starting at a C-rate of 5C, the discharge curves of the LFP_P electrode display a distinct “step.” This characteristic is likely linked to the higher internal resistance of the system and the polarisation phenomenon, requiring additional energy to activate all electrochemically active sites.

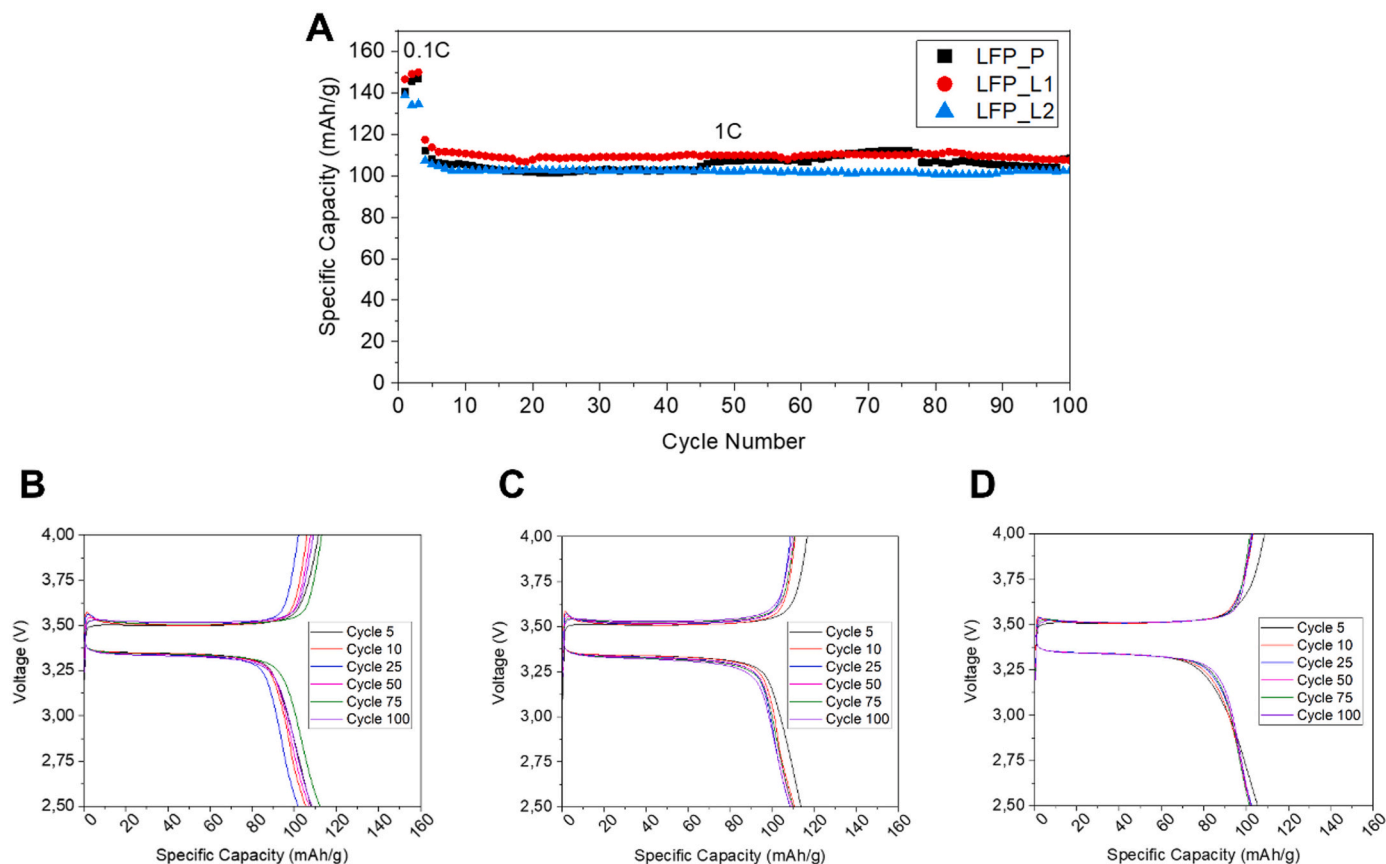
In order to better evaluate the contribution of the current collector, and in particular the effect of the different laser texturing strategies, electrodes with higher mass loading (between 6 and 7 mg cm^{-2}) were tested. The results of the rate capability tests are compared in Fig. 7, while the corresponding specific capacity values are reported in Table 4 for different C-rates.

In this case, the specific capacity was quite similar for the three electrodes. At low C-rates of 0.1C and 0.2C, the performance was comparable, with values of specific capacity close to 145 mAh g^{-1} in all cases (Fig. 7A). The LFP-P electrode exhibited lower coulombic efficiency

Table 5

Values of specific capacity, coulombic efficiency, capacity retention and over potential for LFP_P, LFP_L1 and LFP_L2 electrodes.

Cycle Number	LFP_P				LFP_L1				LFP_L2			
	Specific Capacity	Coulombic Efficiency	Capacity Retention	Over Potential	Specific Capacity	Coulombic Efficiency	Capacity Retention	Over Potential	Specific Capacity	Coulombic Efficiency	Capacity Retention	Over Potential
	mAh g ⁻¹	%	%		mAh g ⁻¹	%	%		mAh g ⁻¹	%	%	
5	107.91	96.76	–	0.16	113.77	97.50	–	0.18	105.51	97.07	–	0.18
10	105.45	99.39	97.72	0.16	110.72	99.72	97.32	0.18	102.54	99.29	97.19	0.18
25	101.88	99.89	94.41	0.17	108.60	99.84	95.46	0.19	102.67	99.60	97.31	0.18
50	107.24	99.48	99.39	0.17	109.85	99.47	96.55	0.20	102.13	99.68	96.80	0.18
75	112.21	99.27	103.98	0.17	110.12	99.48	96.79	0.21	101.62	99.74	96.31	0.18
100	108.46	99.39	100.51	0.19	108.75	99.30	95.59	0.22	102.31	99.76	96.96	0.18

**Fig. 8.** Capacity retention of the three electrodes with different CCs (high mass loading 7 mg cm⁻²) (A), charge/discharge curves for LFP_P (B), charge/discharge curves for LFP_L1 (C), charge/discharge curves for LFP_L2 (D).

during the 5 forming cycles a 0.1C, <95%, while electrodes with laser-textured CCs generally achieved values higher than 99% (Table 5).

At higher C-rates of 10C and 15C, the electrode with the pristine current collector (LFP_P) exhibited similar specific capacity values to LFP_L1 and higher values than LFP_L2. Specifically, LFP_P and LFP_L1 exhibited values of specific capacity close to 50 mAh g⁻¹ at 10C, while LFP_L2 achieved 45 mAh g⁻¹. This trend was more evident at 15C, where LFP_P and LFP_L1 achieved values of specific capacity close to 30 mAh g⁻¹, while LFP_L2 achieved 19 mAh g⁻¹.

These results suggest that having a greater number of closely packed craters on the CC surface does not necessarily lead to better utilisation of the active material, particularly where higher values of mass loading are employed. The more regular treated surface of LFP_L1 instead seemed to enhance the electrochemical performance by providing favourable electron and ion pathways.

To better clarify the role of the specific laser treatment on the cycling stability of cells at higher mass loading, a cycling test at 1C was

conducted on the three electrodes up to 100 cycles. In this case, after three forming cycles at 0.1C, the cells were maintained at a current density of 1C, as reported in Fig. 8.

The electrochemical behaviour of LFP_P, LFP_L1 and LFP_L2 under these conditions was quite similar to that reported previously. As shown in Fig. 8A and Table 5, both LFP_L1 and LFP_L2 exhibited high stability during cycling, whereas LFP_P presented unstable specific capacity.

For cycles 5, 50, and 100, the coulombic efficiency, capacity retention, and over potential were consistent among the three samples, as shown in Table 5. The coulombic efficiency was above 99% for all samples, with this value remaining stable for a higher number of cycles. At the same time, the capacity retention, calculated considering cycle 5 as reference, was over 96% for all three samples. For LFP_P and LFP_L1, a slight increase in over potential could be noted, starting from 0.16 and 0.18 at cycle 5 and reaching 0.19 and 0.22 after 100 cycles, respectively. On the contrary, LFP_L2 exhibited stable values of over potential during cycling, with an average value of 0.18.

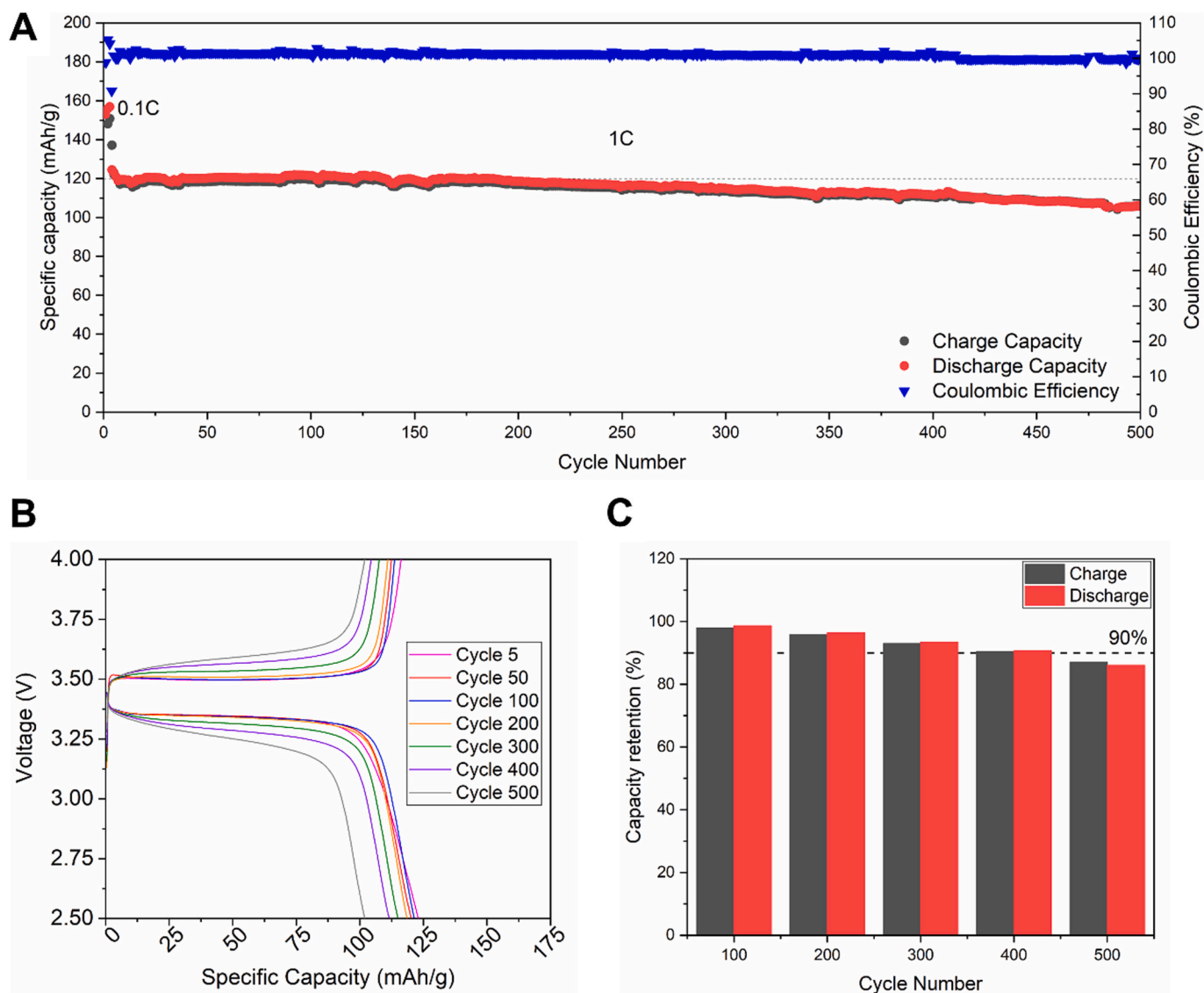


Fig. 9. Long cycling of LFP_L1 half-cell (mass loading 6 mg cm^{-2}) at 1C for 500 cycles (A), charge/discharge curves for LFP_L1 for different cycles (B), capacity retention for different cycles, using as reference the 5th cycles (C).

By taking into consideration the rate capability and cycling stability test results obtained with different mass loadings, the LFP_L1 electrode was selected for electrode optimization and long cycling evaluation. In this case, the electrode mass loading was set to 6 mg cm^{-2} with the cell cycled at a constant rate of 1C for >500 cycles.

As can be observed in Fig. 9, the specific capacity of the LFP_L1 electrode was approximately 150 mAh g^{-1} after three formation cycles at 0.1C with a coulombic efficiency close to 100% at the third cycle, confirming good activation and cycling stability of the cell. Increasing the current by an order of magnitude to 1C, the cell still delivered a specific capacity of 120 mAh g^{-1} with a coulombic efficiency $>99\%$. As can be observed in Fig. 9(A–B), the specific capacity remained close to 120 mAh g^{-1} for >250 cycles, with a capacity retention of 95%. After 500 cycles, the cell still delivered a specific capacity of over 110 mAh g^{-1} , corresponding to a capacity retention of 86%, demonstrating good cycling stability (Fig. 9A–C).

The laser treatment performed on the aluminium CC therefore guaranteed good adhesion of the active material and good electronic transfer, which also affected the long cycling performance of the cell.

4. Conclusions

Nanosecond pulsed laser texturing of LIB CCs presents a unique optimisation problem in which ablation must be exploited to increase the available surface area while the quantity of ejected material must be limited as much as possible to avoid damage. By employing a parallel-line laser scanning strategy with scanning speed and hatch distance chosen to achieve crater separation equal to the focused spot diameter in both directions, a series of adjacent ablation craters was obtained with the crater depth increasing logarithmically with pulse fluence. Optimisation of the laser pulse fluence led to an increase in surface area of 18%. In a second set of laser texturing experiments, the laser fluence was chosen to maximise the aspect ratio of individual craters and the scanning speed and hatch distance were varied over the range 60–120% of the experimental crater diameter. Optimisation of the laser scanning strategy led to a reduction in crater separation and a more closely packed configuration compared to the first set of experiments, achieving increases in surface area of $>30\%$.

Despite the larger increase in surface area obtained upon optimisation of the laser scanning strategy, achieving smaller, more tightly packed ablation craters with higher aspect ratio, textured CCs with such

features did not lead to highest performance during electrochemical tests. These outcomes imply that the developed area ratio (*S_{dr}*), or fraction increase in surface area, while useful for quantifying the increase in surface area following laser texturing, does not provide a complete picture of all factors influencing the performance of laser-textured LIB CCs. In particular, lower values of pulse fluence, scanning speed and hatch spacing led to the formation of smaller closely packed craters with a less defined structure and higher level of disorder, which appeared to at least partially offset benefits in terms of increased surface area. More regular, homogeneous craters with separation equal to the focused laser spot diameter instead led to best performance, ultimately achieving a capacity retention of >86% after 500 cycles. In terms of optimal geometry, the outcomes of this study therefore suggest that laser texturing must result in regular and homogeneous structures with moderate increases in surface area. Further investigation into links between surface topography and electrochemical performance is now required to provide more clear guidelines and key performance indicators for the evaluation of laser texturing of LIB battery current collectors. The outcomes of this investigation nonetheless suggest that laser texturing and, more generally, surface functionalisation, are likely to play important roles in the development of next-generation electric vehicle batteries.

CRediT authorship contribution statement

Elisa Ravasio: Methodology, Investigation, Data curation, Writing – original draft. **Adrian H.A. Lutey:** Conceptualization, Methodology, Investigation, Data curation, Writing – original draft, Funding acquisition. **Daniele Versaci:** Conceptualization, Methodology, Investigation, Data curation, Validation, Writing – original draft. **Luca Romoli:** Conceptualization, Writing – review & editing, Funding acquisition. **Silvia Bodoardo:** Conceptualization, Writing – review & editing, Funding acquisition.

Declaration of Competing Interest

The authors declare that they have no known competing financial interests or personal relationships that could have appeared to influence the work reported in this paper.

Data availability

Data will be made available on request.

Acknowledgements

The authors kindly acknowledge financial support received from the Gigagreen project (Horizon Europe, grant agreement N° 101069707).

Adrian H.A. Lutey received funding from the University of Parma through the action Bando di Ateneo 2022 per la ricerca co-funded by MUR-Italian Ministry of Universities and Research – D.M. 737/2021 - PNR - PNRR – NextGenerationEU for funding. Daniele Versaci acknowledges support from DM 1062/2021 program and Elisa Ravasio acknowledges support from DM 352/2022 program.

Appendix A. Supplementary data

Supplementary data to this article can be found online at <https://doi.org/10.1016/j.susmat.2023.e00751>.

References

- J.T. Frith, M.J. Lacey, U. Ulissi, A non-academic perspective on the future of lithium-based batteries, *Nat. Commun.* 14 (2023) 420, <https://doi.org/10.1038/s41467-023-35933-2>.
- S. Dühnen, J. Betz, M. Kolek, R. Schmich, M. Winter, T. Placke, Toward green battery cells: perspective on materials and technologies, *Small Methods*. 4 (2020) 2000039, <https://doi.org/10.1002/smtd.202000039>.
- M. Fichtner, K. Edström, E. Ayerbe, M. Bercebar, A. Bhowmik, I.E. Castelli, S. Clark, R. Dominko, M. Erakca, A.A. Franco, A. Grimaud, B. Horstmann, A. Latz, H. Lorrmann, M. Meeus, R. Narayan, F. Pammer, J. Ruhland, H. Stein, T. Vegge, M. Weil, Rechargeable batteries of the future—the state of the art from a BATTERY 2030+ perspective, *Adv. Energy Mater.* 12 (2022), <https://doi.org/10.1002/aenm.202102904>.
- H. Jeong, J. Jang, C. Jo, A review on current collector coating methods for next-generation batteries, *Chem. Eng. J.* 446 (2022), <https://doi.org/10.1016/j.cej.2022.136860>.
- D. Li, Q. Lv, C. Zhang, W. Zhou, H. Guo, S. Jiang, Z. Li, The effect of electrode thickness on the high-current discharge and long-term cycle performance of a lithium-ion battery, *Batteries*. 8 (2022), <https://doi.org/10.3390/batteries8080101>.
- D. Versaci, A. Costanzo, S.M. Ronchetti, B. Onida, J. Amici, C. Francia, S. Bodoardo, Ultrasmall SnO₂ directly grown on commercial C45 carbon as lithium-ion battery anodes for long cycling performance, *Electrochim. Acta* 367 (2021), 137489, <https://doi.org/10.1016/j.electacta.2020.137489>.
- P. Zhu, D. Gastol, J. Marshall, R. Sommerville, V. Goodship, E. Kendrick, A review of current collectors for lithium-ion batteries, *J. Power Sources* 485 (2021), <https://doi.org/10.1016/j.jpowsour.2020.229321>.
- C. Heubner, K. Voigt, P. Marcinkowski, S. Reuber, K. Nikolowski, M. Schneider, M. Michaelis, From active materials to battery cells: a straightforward tool to determine performance metrics and support developments at an application-relevant level, *Adv. Energy Mater.* 11 (2021) 2102647, <https://doi.org/10.1002/aenm.202102647>.
- M. Yamada, T. Watanabe, T. Gunji, J. Wu, F. Matsumoto, Review of the design of current collectors for improving the battery performance in Lithium-ion and post-Lithium-ion batteries, *Electrochim. Acta* 1 (2020) 124–159, <https://doi.org/10.3390/electrochem1020011>.
- Y. Yang, W. Yuan, X. Zhang, Y. Ke, Z. Qiu, J. Luo, Y. Tang, C. Wang, Y. Yuan, Y. Huang, A review on structuralized current collectors for high-performance lithium-ion battery anodes, *Appl. Energy* 276 (2020), <https://doi.org/10.1016/j.apenergy.2020.115464>.
- L. Guo, D.B. Thornton, M.A. Koronfel, I.E.L. Stephens, M.P. Ryan, Degradation in lithium ion battery current collectors, *J. Phys. Energy*. 3 (2021), <https://doi.org/10.1088/2515-7655/ac0c04>.
- S. Jin, Y. Jiang, H. Ji, Y. Yu, Advanced 3D current collectors for Lithium-based batteries, *Adv. Mater.* 30 (2018), <https://doi.org/10.1002/adma.201802014>.
- M. Onsrud, A.O. Tezel, S. Fotedar, A.M. Svensson, Novel carbon coating on aluminum current collectors for lithium-ion batteries, *SN Appl. Sci.* 4 (2022), <https://doi.org/10.1007/s42452-022-05103-y>.
- R. Wang, W. Li, L. Liu, Y. Qian, F. Liu, M. Chen, Y. Guo, L. Liu, Carbon black/graphene-modified aluminum foil cathode current collectors for lithium ion batteries with enhanced electrochemical performances, *J. Electroanal. Chem.* 833 (2019) 63–69, <https://doi.org/10.1016/j.jelechem.2018.11.007>.
- I. Doberdo, N. Löffler, N. Laszczynski, D. Cericola, N. Penazzi, S. Bodoardo, G. T. Kim, S. Passerini, Enabling aqueous binders for lithium battery cathodes – carbon coating of aluminum current collector, *J. Power Sources* 248 (2014) 1000–1006, <https://doi.org/10.1016/j.jpowsour.2013.10.039>.
- S. Yoon, H.S. Jang, S. Kim, J. Kim, K.Y. Cho, Crater-like architectural aluminum current collectors with superior electrochemical performance for Li-ion batteries, *J. Electroanal. Chem.* 797 (2017) 37–41, <https://doi.org/10.1016/J.JELECHEM.2017.05.017>.
- S. Pedaballi, C.C. Li, Effects of surface modification and organic binder type on cell performance of water-processed Ni-rich Li(Ni_{0.8}Co_{0.1}Mn_{0.1})O₂ cathodes, *J. Power Sources* 472 (2020), <https://doi.org/10.1016/j.jpowsour.2020.228552>.
- W. Pflöging, Recent progress in laser texturing of battery materials: a review of tuning electrochemical performances, related material development, and prospects for large-scale manufacturing, *Int. J. Extreme Manuf.* 3 (2021), <https://doi.org/10.1088/2631-7990/abca84>.
- W. Pflöging, A review of laser electrode processing for development and manufacturing of lithium-ion batteries, *Nanophotonics*. 7 (2017) 549–573, <https://doi.org/10.1515/nanoph-2017-0044>.
- N. Khosla, J. Narayan, R. Narayan, X.G. Sun, M.P. Paranthaman, Microstructure and defect engineering of graphite anodes by pulsed laser annealing for enhanced performance of lithium-ion batteries, *Carbon N Y* 205 (2023) 214–225, <https://doi.org/10.1016/J.CARBON.2023.01.009>.
- N. Khosla, J. Narayan, R. Narayan, X.-G. Sun, M.P. Paranthaman, Nanosecond laser annealing of NMC 811 cathodes for enhanced performance, *J. Electrochem. Soc.* 170 (2023), 030520, <https://doi.org/10.1149/1945-7111/ACC27D>.
- Y. Wang, Z. Zhao, J. Zhong, T. Wang, L. Wang, H. Xu, J. Cao, J. Li, G. Zhang, H. Fei, J. Zhu, Hierarchically Micro/nanostructured current collectors induced by ultrafast femtosecond laser strategy for high-performance Lithium-ion batteries, *Energy Environ. Mater.* (2021), <https://doi.org/10.1002/eem2.12223>.
- X.X. Tang, W. Liu, B.Y. Ye, Y. Tang, Preparation of current collector with blind holes and enhanced cycle performance of silicon-based anode, *Trans. Nonferrous Metals Soc. China (Eng. Ed.)* 23 (2013) 1723–1727, [https://doi.org/10.1016/S1003-6326\(13\)62654-0](https://doi.org/10.1016/S1003-6326(13)62654-0).
- Y. Zheng, Z. An, P. Smyrek, H.J. Seifert, T. Kunze, V. Lang, A.-F. Lasagni, W. Pflöging, Direct laser interference patterning and ultrafast laser-induced micro/nano structuring of current collectors for lithium-ion batteries, in: *Laser-Based Micro- and Nanoprocessing X*, SPIE, 2016, p. 97361B, <https://doi.org/10.1117/12.2220111>.

- [28] L. Romoli, A.H.A. Lutey, G. Lazzini, Laser texturing of Li-ion battery electrode current collectors for improved active layer interface adhesion, *CIRP Ann.* (2022), <https://doi.org/10.1016/j.cirp.2022.04.034>.
- [29] A.H.A. Lutey, L. Romoli, Surface topography following pulsed laser texturing: implications for adhesion and wettability, *Surf. Topogr.* 7 (2019), <https://doi.org/10.1088/2051-672X/ab5c82>.
- [30] D. Kim, N.M. Pugno, S. Ryu, Wetting theory for small droplets on textured solid surfaces, *Sci. Rep.* 6 (2016), <https://doi.org/10.1038/srep37813>.
- [31] J. Drelich, E. Chibowski, Superhydrophilic and superwetting surfaces: definition and mechanisms of control, *Langmuir.* 26 (2010) 18621–18623, <https://doi.org/10.1021/la1039893>.
- [32] Z. Du, K.M. Rollag, J. Li, S.J. An, M. Wood, Y. Sheng, P.P. Mukherjee, C. Daniel, D. L. Wood, Enabling aqueous processing for crack-free thick electrodes, *J. Power Sources* 354 (2017) 200–206, <https://doi.org/10.1016/J.JPOWSOUR.2017.04.030>.
- [33] J. Li, C. Daniel, D. Wood, Materials processing for lithium-ion batteries, *J. Power Sources* 196 (2011) 2452–2460, <https://doi.org/10.1016/J.JPOWSOUR.2010.11.001>.
- [34] C.V. Ngo, D.M. Chun, Control of laser-ablated aluminum surface wettability to superhydrophobic or superhydrophilic through simple heat treatment or water boiling post-processing, *Appl. Surf. Sci.* 435 (2018) 974–982, <https://doi.org/10.1016/J.APSUSC.2017.11.185>.
- [35] D. Lou, T. Li, E. Liang, B. Lin, W.-X. He, L.-W. Jiang, Y. Lai, J. Huang, J. Guo, Z. Yang, J. Zhao, Effect of nanosecond laser treatment parameters on surface wettability behaviour of pure aluminium, *IOP Conf. Ser. Mater Sci. Eng.* 538 (2019), <https://doi.org/10.1088/1757-899X/538/1/012021>, 012021.